

# Mineralization-Inspired Synthesis of Magnetic Zeolitic Imidazole Framework Composites

Anastasia Terzopoulou<sup>+</sup>, Marcus Hoop<sup>+</sup>, Xiang-Zhong Chen,<sup>\*</sup> Ann M. Hirt, Michalis Charilaou, Yang Shen, Fajer Mushtaq, Angel Pérez del Pino, Constantin Logofatu, Laura Simonelli, Andrew J. de Mello, Christian J. Doonan, Jordi Sort, Bradley J. Nelson, Salvador Pané,<sup>\*</sup> and Josep Puigmartí-Luis<sup>\*</sup>

**Abstract:** Metal–organic frameworks (MOFs) capable of mobility and manipulation are attractive materials for potential applications in targeted drug delivery, catalysis, and small-scale machines. One way of rendering MOFs navigable is incorporating magnetically responsive nanostructures, which usually involve at least two preparation steps: the growth of the magnetic nanomaterial and its incorporation during the synthesis of the MOF crystals. Now, by using optimal combinations of salts and ligands, zeolitic imidazolate framework composite structures with ferrimagnetic behavior can be readily obtained via a one-step synthetic procedure, that is, without the incorporation of extrinsic magnetic components. The ferrimagnetism of the composite originates from binary oxides of iron and transition metals such as cobalt. This approach exhibits similarities to the natural mineralization of iron oxide species, as is observed in ores and in biomineralization.

## Introduction

The mineralization of magnetic iron compounds is ubiquitous in nature. Aside from their occurrence in geological materials, iron-based magnetic minerals can be found



in a wide variety of organisms, ranging from bacteria to vertebrates.<sup>[1]</sup> Biogenic magnets serve as receptors of the Earth's magnetic field, allowing organisms to navigate. Mineralization of magnetic mass occurs in a dynamic environment where several chemical reactions take place simultaneously. Inspired by these naturally occurring processes, we have designed a direct approach in which the mineralization of magnetic material is concomitant to the growth of a MOF (Figure 1).

There are many reports of methods showing the fabrication of magnetically active MOF composites.<sup>[2]</sup> These methods can be basically divided into two categories: 1) in situ encapsulation of magnetic nanostructures within the frameworks during their growth; and 2) decoration of magnetic architectures with MOF shells (or coatings). A relevant example of the first approach is the MOF nanocomposite reported by Huo and co-workers, in which superparamagnetic magnetite nanoparticles are encapsulated within ZIF-8 crystals during their growth.<sup>[3]</sup> A recent example of the second strategy is the MOFBOTs reported by Puigmartí-Luis, Pané, and co-workers.<sup>[4]</sup> The authors reported on magnetically driven helical microrobots, whose surface was decorated with ZIF-8. Note that all these approaches require the extrinsic use

[\*] A. Terzopoulou,<sup>[†]</sup> Dr. M. Hoop,<sup>[†]</sup> Dr. X.-Z. Chen, F. Mushtaq, Prof. B. J. Nelson, Dr. S. Pané  
Multi-Scale Robotics Lab (MSRL)  
Institute of Robotics and Intelligent Systems (IRIS), ETH Zurich  
Tannenstrasse 3, 8092 Zurich (Switzerland)  
E-mail: chenxian@ethz.ch  
vidalp@ethz.ch  
Prof. A. M. Hirt  
Institute of Geophysics, ETH Zurich  
Sonnegstrasse 5, 8092 Zurich (Switzerland)  
Dr. M. Charilaou  
Laboratory of Metal Physics and Technology  
Department of Materials, ETH Zurich  
Vladimir Prelog Weg 1, 8093 Zurich (Switzerland)  
Dr. Y. Shen  
Institute of Food, Nutrition and Health, ETH Zurich  
Schmelzbergstrasse 7, 8092 Zurich (Switzerland)  
Dr. A. P. del Pino  
Institute of Materials Science of Barcelona (ICMAB-CSIC)  
Campus UAB, 08193 Bellaterra (Spain)  
Dr. C. Logofatu  
National Institute for Materials Physics  
PO Box MG 7, 77125 Bucharest (Romania)

Dr. L. Simonelli  
CELLS—ALBA Synchrotron Radiation Facility  
Carrer de la Llum 2–26, 08290 Cerdanyola del Valles  
Barcelona (Spain)  
Prof. A. J. de Mello, Dr. J. Puigmartí-Luis  
Institute of Chemical and Bioengineering, ETH Zurich  
Vladimir Prelog Weg 1, 8093 Zurich (Switzerland)  
E-mail: josep.puigmarti@chem.ethz.ch  
Prof. C. J. Doonan  
School of Chemistry and Physics, University of Adelaide  
South Australia 5005 (Australia)  
Prof. J. Sort  
Institutació Catalana de Recerca i Estudis Avançats (ICREA) and  
Departament de Física, Universitat Autònoma de Barcelona  
08193 Bellaterra (Spain)

[†] These authors contributed equally to this work.

 Supporting information and the ORCID identification number(s) for the author(s) of this article can be found under:  
 <https://doi.org/10.1002/anie.201907389>.

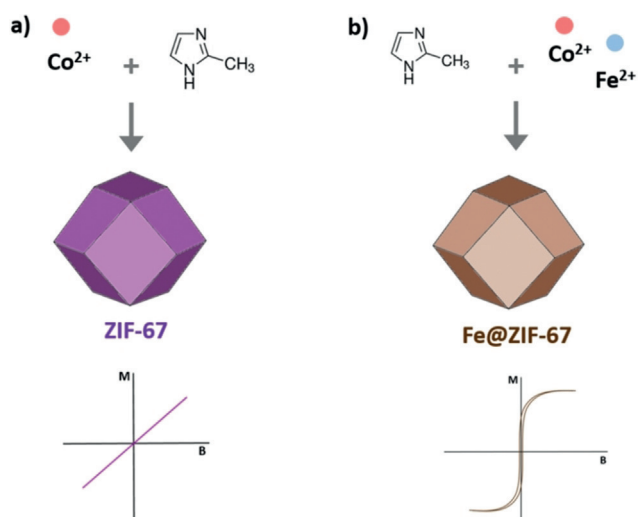


**Figure 1.** Illustration showing the synthesis of a) ZIF-67 and b) Fe@ZIF-67. While (a) renders paramagnetic MOF crystals, (b) results in a ferrimagnetic composite.

of magnetic components, which differ from the approach hereby presented.

## Results and Discussion

We used a well-established procedure for the synthesis of cobalt-based ZIF-67,<sup>[5]</sup> only modified by the addition of ferrous salts in the MOF reaction medium. The addition of iron(II) sulfate to the MOF precursor solution leads to the formation of a magnetically active material we term Fe@ZIF-67. Unlike ZIF-67, Fe@ZIF-67 structures can be readily collected by a magnet on short timescales (Figure 2a; Supporting Information, Video S1).

To assess whether Fe@ZIF-67 preserves MOF-like characteristics, we first conducted scanning electron microscopy (SEM), transmission electron microscopy (TEM), Brunauer–Emmett–Teller (BET) surface area analysis, and X-ray diffraction (XRD) measurements of both ZIF-67 and Fe@ZIF-67. Figure 2b shows an SEM image of a Fe@ZIF-67 particle of rhombic dodecahedral shape, which is also typical for ZIF-67 (Figure 2c). However, Fe@ZIF-67 exhibits distinct morphological features with respect to ZIF-67, such as a rougher surface and smaller average particle size (Supporting Information, Figure S1). High-angle annular dark-field (HAADF) TEM images indicate the formation of fiber-like structures within Fe@ZIF-67 (observed as dark contrast regions in Figure 2d) that are not observed in pristine ZIF-67 (Figure 2e).

Next, we assessed the compositional distribution of elements in Fe@ZIF-67 by means of EDX analysis in high-resolution TEM (HRTEM). The presence of C, N, Co, Fe, and O were confirmed, with Fe and O primarily localized in the fiber-like structures (Figure 2f; Supporting Information, Figure S2). The ratio of Fe and Co is close to one, as determined by Rutherford backscattering spectroscopy (RBS; Supporting Information, Figure S3). Interestingly, the formation of cav-

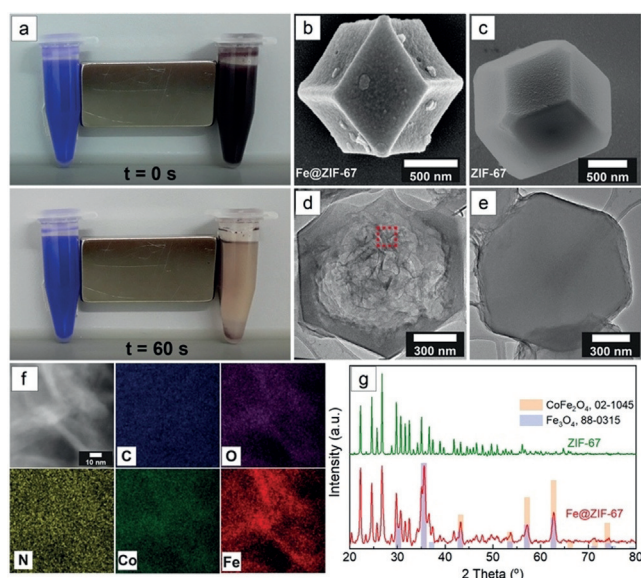


**Figure 2.** Comparison of ZIF-67 and magnetic Fe@ZIF-67 in terms of their magnetotacticity, morphology, and crystalline structures. a) Time-lapse images showing that Fe@ZIF-67 (brown sample on the right) can be collected by a magnet within 60 s, while pristine ZIF-67 cannot (violet sample on the left). b), c) SEM images of the magnetic Fe@ZIF-67 (b) and the pristine ZIF-67 (c). d), e) TEM images of the magnetic Fe@ZIF-67 (d) and the pristine ZIF-67 (e). f) The magnified image of the region marked by the red box in (d), and the corresponding elemental distribution of the same region obtained with EDX mapping. g) XRD patterns of the magnetic Fe@ZIF-67 and the pristine ZIF-67. The reference patterns of Fe<sub>3</sub>O<sub>4</sub> and CoFe<sub>2</sub>O<sub>4</sub> are indicated by the violet and orange bars.

ities was observed in a significant number of Fe@ZIF-67 particles (Supporting Information, Video S2, HRTEM tomography). To date, cavity formation in MOFs has been mostly achieved via multi-step processes,<sup>[6]</sup> with a few exceptions that include solvothermal treatments.<sup>[7]</sup>

BET measurements revealed the porous nature of Fe@ZIF-67. As expected, the specific surface area of the Fe@ZIF-67 composite (ca. 900 m<sup>2</sup>g<sup>−1</sup>) is lower than that of pristine ZIF-67 (1600 m<sup>2</sup>g<sup>−1</sup>; Supporting Information, Figure S4). Furthermore, the isotherm of Fe@ZIF-67 shows a small hysteresis loop, which is characteristic of imperfections in the microporous network; as evidenced by SEM and TEM images. Calculations of the pore-width distribution revealed a bimodal distribution with two average pore sizes of 1 nm and 1.45 nm for both ZIF-67 and Fe@ZIF-67 (Supporting Information, Figure S5). XRD analysis confirms that Fe@ZIF-67 incorporates the crystalline structure of ZIF-67 (Figure 2g). However, additional peaks are found at 35.6°, 43.2°, 53.7°, 57.2°, and 62.7°, which are characteristic of magnetic spinel oxides such as Fe<sub>3</sub>O<sub>4</sub> (JCPDS:88–0315) and CoFe<sub>2</sub>O<sub>4</sub> (JCPDS:02–1045). Therefore, our approach is the first reported example of organomineralization in MOF chemistry. Note that organomineralization is a term proposed by Perry et al.,<sup>[8]</sup> which refers to a process where minerals are precipitated in a non-biological organic milieu (for example, synthetic organic compounds, organopolymers) and without an obvious biological control. In contrast to our approach,

current methods employed for the synthesis of magnetically active MOF composites involve: multiple steps, longer reaction times, use of toxic solvents, inert atmosphere conditions, or high-temperature treatments.<sup>[2b,9]</sup>

The magnetic behavior of the Fe@ZIF-67 composite was investigated by several magnetic methods. As shown in Figure 3a, the magnetization curve of ZIF-67 indicate paramagnetic behavior, that is, a linear relationship between the

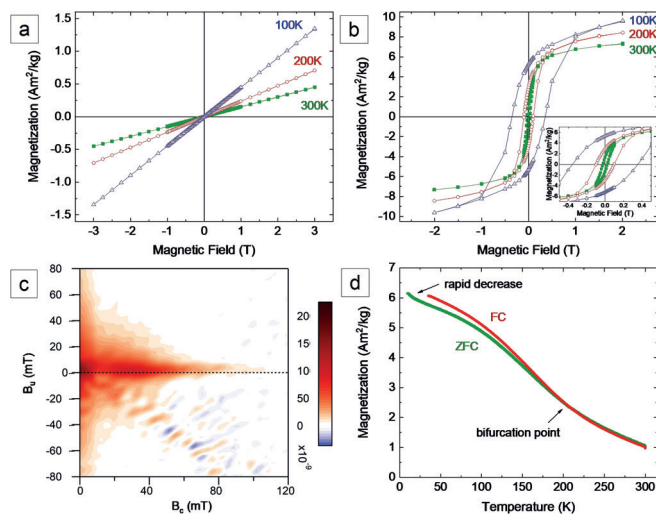


**Figure 3.** Magnetic properties of pristine ZIF-67 and magnetic Fe@ZIF-67. a,b) Magnetization curves of pristine ZIF-67 (a) and magnetic Fe@ZIF-67 (b) measured at different temperatures (100 K, 200 K, 300 K), respectively. c) FORC measurement at room temperature of the magnetic Fe@ZIF-67, in which  $B_c$  shows the coercivity spectrum, and  $B_u$  indicates the range of interaction fields. d) temperature dependent remnant magnetization of the magnetic Fe@ZIF-67.

magnetic moment and the applied field, even at low temperatures. The increase in the gradient of the magnetic moment (that is, susceptibility) as a function of inverse temperature also confirms that the magnetization is pure paramagnetism in origin. In contrast, Fe@ZIF-67 exhibits ferrimagnetism at room temperature (Figure 3b) with a coercive field of 0.024 T and remnant magnetization of  $1.34 \text{ Am}^2 \text{ kg}^{-1}$ . A decrease in temperature results in an increase in the remnant magnetic moment and coercivity. A linear background is superimposed to the ferrimagnetic contribution at all temperatures. This feature is most likely caused by the paramagnetic contribution of the ZIF-67 structure. It should be noted that uncompensated spins inside or at the surface of the magnetic particles, such as iron oxyhydroxides, may also contribute to this phenomenon.<sup>[10]</sup> Importantly, the hysteresis loops of Fe@ZIF-67 reveal information about their composition. Indeed, we have observed that the obtained average value of the saturation magnetization ( $M_s$ ) from replicas of Fe@ZIF-67 from 5 different batches at room temperature was  $5.0 \pm 0.5 \text{ Am}^2 \text{ kg}^{-1}$ . This value indicates that the variability of the magnetic material in the MOF composite is low (see the Supporting Information for a detailed calculation of the magnetic composition).

To shed more light on the distinct magnetic properties observed in Fe@ZIF-67, we performed first-order reversal curve (FORC) analysis and temperature dependent (10–300 K) field-cooled (FC) and zero-field-cooled (ZFC) magnetization experiments. FORC measurements provide information about the distribution of coercive and interaction fields of magnetic components, and therefore they can be used to identify different magnetic behaviors within a magnetic sample.<sup>[11]</sup> A FORC diagram is based on multiple partial hysteresis curves. Briefly, the sample is initially brought to saturation under a large positive magnetic field. Next, the field is decreased to a reversal field  $B_A$ , which is the starting point of a partial hysteresis. Then, the magnetic field is being swept from  $B_A$  to the positive saturation field. The magnetic moment recorded at a certain field  $B_B > B_A$  for the specific partial hysteresis is denoted as  $M(B_A, B_B)$ . The FORC distribution  $\rho(B_A, B_B)$  is determined as follows [Eq. (1)]:

$$\rho(B_A, B_B) = -\frac{\partial^2 M(B_A, B_B)}{\partial B_A \partial B_B} \quad (1)$$

Accordingly, the FORC distribution can be plotted in the field space as a function of  $B_A$  and  $B_B$  or by changing coordinates  $B_u = (B_A + B_B)/2$  and  $B_c = (B_B - B_A)/2$ . This change of the coordinates introduces an axis rotation, and since  $B_B > B_A$ , the FORC diagram is then confined to the  $B_c > 0$  plane. In this case,  $B_c$  shows the coercivity spectrum, and  $B_u$  indicates the range of interaction fields. The simplest case of an isolated single domain particle would contribute to this diagram at the position  $B_u = 0$  and  $B_c$  equal to the switching field. For an assemble of single domain particles interacting with each other, a vertical spread over  $B_u$  would be observed. In our case, as shown in Figure 3c, the FORC diagram of Fe@ZIF-67 measured at room temperature indicates the presence of components with two different magnetic responses. A peak close to the origin and shifted slightly upwards along the interaction axis indicates the existence of components exhibiting superparamagnetic (SP) behavior with a very low coercivity ( $B_c$ ).<sup>[11a]</sup> A second family of components is characterized by an elongated distribution between 20 to 60 mT (with a limited vertical spread), suggesting the presence of single-domain particles with minimal interaction between them. The broad distribution can be attributed to the presence of different sizes or compositions of magnetic components present in Fe@ZIF-67. Additionally, a ridge can be observed along the  $135^\circ$  direction, which is indicative of an exchange interaction between two types of magnetic matter (superparamagnetic and ferrimagnetic) with distinct coercivities.<sup>[12]</sup>

The temperature-dependent (10–300 K) zero-field-cooled (ZFC) and field-cooled (FC) remnant magnetization curves of Fe@ZIF-67 are shown in Figure 3d. In ZFC mode, the sample was first cooled from 300 K to 10 K without an applied magnetic field. A magnetic field of 2 T was then applied at 10 K to magnetize the sample, and the change in remnant magnetic moment ( $m_{\text{rem}}$ ) monitored upon heating to room temperature. For the FC measurement, the sample was cooled to 10 K at a constant magnetic field of 2 T and subsequently heated to room temperature with no applied magnetic field.



The slight difference between FC and ZFC curves can be explained by the fact that certain magnetic components in Fe@ZIF-67 composites acquire a remnant magnetization, while the system experiences partial magnetic blocking during FC. Below 30 K, ZFC thermal demagnetization curves show a steep decrease with increasing temperature, indicating a rapid unblocking of magnetization upon heating. Such rapid unblocking behavior in this temperature range has been observed in ferric oxyhydroxides, such as ferrihydrite, with very small crystal sizes.<sup>[10,13]</sup> Demagnetization reduces upon further heating, indicating that there exists a magnetic component whose magnetization is gradually unblocked over the entire measured temperature range. ZFC and FC curves merge at 205 K, after which the magnetization continues to drop with increasing temperature. The non-zero remnant magnetization at room temperature is in line with the results presented in Figure 3b, indicating there is a fraction of material which is still blocked at room temperature. This is corroborated by the FC and ZFC curves under low magnetic field (10 mT; Supporting Information, Figure S6), where it can be clearly seen that both curves do not merge completely at temperatures below room temperature. The occurrence of two magnetic counterparts with distinct blocking temperature is in line with the FORC results.

XRD measurements implied the presence of ferrimagnetic materials such as magnetite and cobalt ferrite within the ZIF network. However, the diffraction patterns of these two species are too similar (Figure 2g) to determine whether Co is incorporated into the spinel metal oxides to form  $\text{Co}_x\text{Fe}_{3-x}\text{O}_4$ . Regardless, the formation of ferrihydrites is highly possible, as inferred from the ZFC and FC curves. Additionally, XRD patterns of ferrihydrites display two weak reflections at  $35.8^\circ$  and  $62.9^\circ$ , which coincide with peaks corresponding to cobalt ferrite and magnetite. To further investigate the magnetic material formed in Fe@ZIF-67 composites, we performed X-ray absorption near-edge structure (XANES) analysis on ZIF-67 and Fe@ZIF-67 at the Co and Fe K-edges, and compared the results with XANES spectra of reference species (for example,  $\text{CoFe}_2\text{O}_4$ ,  $\text{Fe}_3\text{O}_4$ , or ferrihydrite). The Co K-edge absorption spectrum of ZIF-67 crystals displays a pre-edge peak at approximately 7709 eV (Figure 4a). This peak can be ascribed to the dipole forbidden transition from the 1s to 3d states in  $\text{Co}^{\text{II}}$  ions, and is due to p–d mixing in the non-centrosymmetric tetrahedral ligand-field geometry. Fe@ZIF-67 composite structures exhibit a peak at the same position, indicating that cobalt remains in the +2 oxidation state of  $\text{Co}^{\text{II}}$ , as it is also found in ZIF-67.<sup>[14]</sup> Since the pre-edge peak is a measure of the ligand-field strength of  $\text{Co}^{\text{II}}$  ions with a tetrahedral ligand-field geometry, the decrease in peak intensity can be attributed to the loss of  $\text{Co}^{\text{II}}$  with this coordination symmetry. In line with this assumption, we observed differences in the intensity of the peaks located at 7727.7 eV and 7732 eV when comparing ZIF-67 and Fe@ZIF-67. These two peaks correspond to the 1s–4p white-line transition and are indicative of the coordination number of  $\text{Co}^{\text{II}}$  ions. In Fe@ZIF-67, the intensity of the peak at 7727.7 eV increases, whereas the peak at 7732 eV decreases, suggesting that  $\text{Co}^{\text{II}}$  ions increase their coordination number to 6. Both, pre-edge and the white line transition peaks confirm the

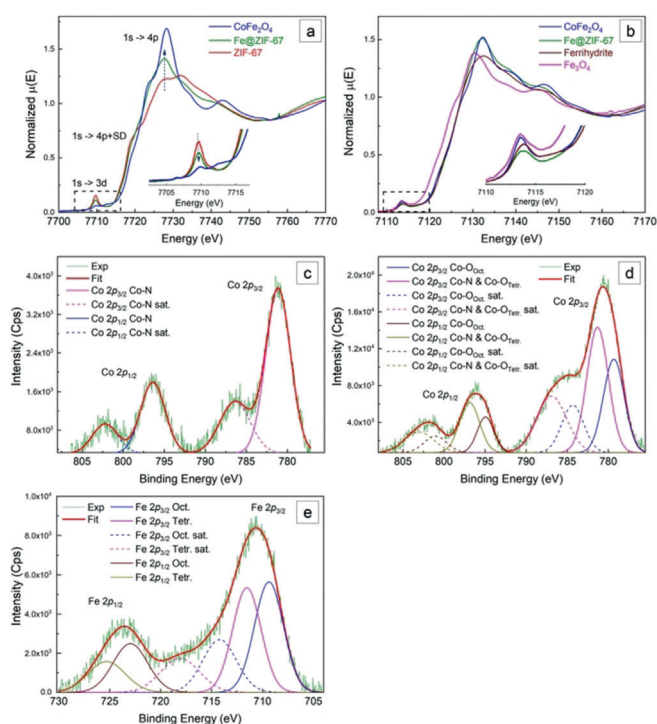


**Figure 4.** Structural origin of ferrimagnetism in the Fe@ZIF-67.

a), b) Normalized XANES spectra at Co K-edge for the Fe@ZIF-67 and reference samples (cobalt ferrite and ZIF-67) (a) and at Fe K-edge for the Fe@ZIF-67 and reference samples (cobalt ferrite, ferrihydrite and magnetite) (b). Insets show the magnified plots of the pre-edge peak regions. c)–e) High-resolution XPS spectra of Co 2p of the ZIF-67 (c), Co 2p of the Fe@ZIF-67 (d), and Fe 2p of the Fe@ZIF-67 (e). Dashed lines correspond to shake-up satellite peaks.

change in the coordination number and indicate that  $\text{Co}^{\text{II}}$  can be incorporated into spinel oxides, such as cobalt ferrite, where  $\text{Co}^{\text{II}}$  tends to occupy the octahedral sites. This hypothesis is supported by comparing the linear combination of the XANES spectra of ZIF-67 and the cobalt ferrite control sample with the XANES spectrum of the Fe@ZIF-67 (Supporting Information, Figure S7).

Figure 4b shows XANES spectra of Fe@ZIF-67,  $\text{CoFe}_2\text{O}_4$ ,  $\text{Fe}_3\text{O}_4$ , and ferrihydrite at the Fe K-edge. From the position of the rising edge, we are able to conclude that Fe in Fe@ZIF-67 is predominantly in a +3 oxidation state. The pre-edge peak of Fe@ZIF-67 is located between the pre-edge peaks of ferrihydrite and  $\text{CoFe}_2\text{O}_4$ , and it appears flatter and broader than the other two. The pre-edge absorption peak position and intensity of  $\text{Fe}^{\text{III}}$  ion is highly related to its coordination geometry.<sup>[15]</sup> In general, the pre-edge absorption peak of  $\text{Fe}^{\text{III}}$  in 4-coordinated geometry (square planar and tetrahedral coordination geometries) is expected at slightly lower energy position than that of octahedral coordination. Besides, 4-coordinated Fe ions show higher intensities than 6-coordinated ones. In  $\text{CoFe}_2\text{O}_4$  and ferrihydrite, the  $\text{Fe}^{\text{III}}$  ions can be either tetrahedrally or octahedrally coordinated, and in ferrihydrite it is believed that the tetrahedrally coordinated ones are much less common than the octahedrally coordinated ones.<sup>[16]</sup> The position, intensity, and broader shape of the Fe@ZIF-67 pre-edge peak indicates a convolution of

more than one contribution, suggesting a mixed tetrahedral and octahedral environment. The XANES spectrum of Fe@ZIF-67 tallies with a linear combination of the XANES spectra of ferrihydrite and  $\text{CoFe}_2\text{O}_4$  (Supporting Information, Figure S8). It should be noted that the composite has a complex structure with a wide range of composition distribution, as indicated by the magnetic characterization. We assume that the crystalline structures exhibit local defects, and, as a consequence, the crystal lattices experience distortion. Therefore, the spectrum of the sample cannot be fitted perfectly by linear combination of the spectra of the commercial reference samples.

X-ray photoelectron spectroscopy (XPS) also confirms the coordination between Co and O. The Co 2p peaks of the pristine ZIF-67 can be deconvoluted into several components, that is, the  $2p_{3/2}$  peak (781.1 eV),  $2p_{1/2}$  peak (796.3 eV), and their satellite peaks (Figure 4c).<sup>[14b]</sup> For Fe@ZIF-67, the Co 2p peaks show a broadening and shift towards lower binding energies, which is related to the formation of Co–O coordination (Figure 4d). The Co  $2p_{3/2}$  peak in the Fe@ZIF-67 could be further deconvoluted into two peaks at 781.3 eV and 779.3 eV, respectively. The peak at 781.3 eV may not only result from the contribution of Co–N coordination but also from the Co–O with a tetrahedral configuration (as these two peaks are very close). The peak at 779.3 eV can be assigned to  $\text{Co}^{\text{II}}$  ions occupying octahedral sites in cobalt ferrite. Similar results are also observed for the Co  $2p_{1/2}$  peak and the satellite peaks. The high resolution spectrum of Fe 2p (Figure 4e) reveals the two spin-orbit doublets Fe  $2p_{3/2}$  (709.4 eV, octahedrally coordinated  $\text{Fe}^{\text{III}}$ ) and 711.6 eV, tetrahedrally coordinated  $\text{Fe}^{\text{III}}$ ), Fe  $2p_{1/2}$  (723.0 eV octahedrally coordinated  $\text{Fe}^{\text{III}}$  and 725.2 eV tetrahedrally coordinated  $\text{Fe}^{\text{III}}$ ) and the shake-up satellites (714.3 eV and 718.6 eV). However, it is not possible to distinguish between contributions from cobalt ferrite and ferrihydrite to these peaks, since both compounds include octahedrally and tetrahedrally coordinated  $\text{Fe}^{\text{III}}$ .<sup>[16b,17]</sup>

As noted, mobile magnetic MOF network composites offer unique features for a wide range of applications such as targeted drug delivery, small-scale robotics, microfluidics and catalysis.<sup>[2b,18]</sup> Over the past years, MOFs have been used for drug delivery applications, since they are able to accommodate therapeutic agents in their structure. However, their potential as gene carriers has been rarely investigated.<sup>[19]</sup> Besides, the delivery of their cargo payloads usually rely on the passive accumulation to a target site.<sup>[19b]</sup> To this end, we have demonstrated the feasibility of gene delivery using magnetically responsive Fe@ZIF-67-based microtransporters. Our results indicate that the use of magnetic fields when incubating cells with Fe@ZIF-67 microcarriers loaded with plasmid DNA enhance gene transfection. DNA plasmids encoding for green fluorescence protein (GFP) can be loaded on the magnetic Fe@ZIF-67 and conveyed to human embryonic kidney (HEK) cells (Supporting Information, Figure S9). Bare plasmid exhibits a transfection efficiency of only 0.4 %. Applying Fe@ZIF-67 loaded with 100 ppm plasmid to HEK cells showed an increase in transfection efficiency of 4.3 %. The elevated transfection performance in this case can be attributed to the sedimentation of the structure with subsequent cellular uptake (for example, phagocytosis). Strikingly,

under magnetic manipulation 13.6% of the cells were transfected with the same concentration of Fe@ZIF-67 and plasmid. These results clearly demonstrate that magnetically responsive MOFs are potential candidates for biomedical applications.

## Conclusion

Our in-depth characterization of Fe@ZIF-67 revealed that the observed magnetic response originates from an organo-mineralization process leading to a single-domain ferrimagnetic component, which is still blocked at room temperature, and a superparamagnetic ferrite within the MOF network, which only undergoes blocking below 205 K. The broad coercivity distribution displayed in the FORC diagrams and the gradual unblocking behavior over a wide range of temperatures provide clear evidence of the rich nature of the current system in terms of both composition and size distribution. The formation of complex heterogeneous systems, especially in Fe-containing minerals, has been widely observed in natural geological and artificial mineralization processes. In this respect, ferrihydrite ( $\text{Fe}_2\text{O}_3 \cdot y\text{H}_2\text{O}$ ), while not contributing to room-temperature ferrimagnetism, can play a key role in the formation of other iron-containing oxides.<sup>[20]</sup> The addition of transition-metal ions can change the reaction kinetics of the transformation of ferrihydrite to other iron oxides and facilitate the crystallization of the spinel phase.<sup>[21]</sup> Accordingly, it is highly plausible that the ferrihydrite formed in the MOF reaction media constitutes a chemogenic source for the subsequent formation of spinel magnetic mass within the ZIF network. However, the possibility cannot be excluded that the spinel phase may also nucleate near the surface of intermediate species such as  $\text{Fe}(\text{OH})_2$  or  $\text{Co}(\text{OH})_2$ , as observed in previous investigations.<sup>[21b,22]</sup>

In summary, our approach is a one-pot synthetic mild process conducted in water and at ambient temperature and pressure. Importantly, the basic pH conditions of the as-prepared solution facilitates the concomitant formation of iron- and cobalt-based oxides. Consequently, this approach can be considered the first reported example of organo-mineralization exploited for the production of magnetic MOF composites, which has the potential to be adapted to other MOF systems. Finally, additional preliminary investigations indicate that by employing the strategy presented herein, magnetic framework composites can also be obtained for ZIF-8 ( $\text{Zn}(\text{mIM})_2$ , zeolite net: SOD) and ZIF-14 ( $\text{Zn}(\text{eIM})_2$ , zeolite net: ANA)<sup>[23]</sup> (Supporting Information, Figures S10, S11, Videos S3, S4). This facile approach will create new opportunities for producing ferrimagnetic MOF-based composites for a wealth of applications.

## Acknowledgements

This work was financed by the European Research Council Starting Grant ELECTROCHEMBOTS (ERC-2013-STG No. 336456), microCrysFact (ERC-2015-STG No. 677020), ETH Grant Mofbots (No. ETH-33 17-1), the Swiss National

Science Foundation (project no. 200021\_181988), and ETH Career Seed Grant (No. SEED-14 16-1). The authors would like to acknowledge Lydia Zehnder from Institute für Geochemie und Petrologie of ETH for her kind support on XRD measurements. Partial financial support from the 2017-SGR-292 project (Generalitat de Catalunya) and the MAT2017-86357-C3-1-R project (and associated Feder) from the Spanish Government is also acknowledged. The XAS experiments were performed at BL22 CLÆSS beamline at ALBA Synchrotron with the collaboration of ALBA staff. The authors would also like to acknowledge the Scientific Center for Optical and Electron Microscopy (ScopeM) and FIRST laboratory of ETH for their technical support.

### Conflict of interest

The authors declare no conflict of interest.

**Keywords:** biomedical applications · magnetism · metal–organic frameworks · zeolitic imidazolate frameworks

**How to cite:** *Angew. Chem. Int. Ed.* **2019**, *58*, 13550–13555  
*Angew. Chem.* **2019**, *131*, 13684–13689

- [1] a) R. Blakemore, *Science* **1975**, *190*, 377; b) D. R. Lovley, J. F. Stolz, G. L. Nord, E. J. P. Phillips, *Nature* **1987**, *330*, 252; c) D. A. Bazylinski, R. B. Frankel, H. W. Jannasch, *Nature* **1988**, *334*, 518.
- [2] a) S. S. Nadar, N. V. O. S. Suresh, P. Rao, D. J. Ahirrao, S. Adsare, *J. Taiwan Inst. Chem. Eng.* **2018**, *91*, 653; b) R. Ricco, L. Malfatti, M. Takahashi, A. J. Hill, P. Falcaro, *J. Mater. Chem. A* **2013**, *1*, 13033.
- [3] G. Lu, S. Li, Z. Guo, O. K. Farha, B. G. Hauser, X. Qi, Y. Wang, X. Wang, S. Han, X. Liu, J. S. DuChene, H. Zhang, Q. Zhang, X. Chen, J. Ma, S. C. J. Loo, W. D. Wei, Y. Yang, J. T. Hupp, F. Huo, *Nat. Chem.* **2012**, *4*, 310.
- [4] X. Wang, X.-Z. Chen, C. Alcantara, S. Sevim, M. Hoop, A. Terzopoulou, C. de Marco, C. Hu, A. J. deMello, P. Falcaro, S. Furukawa, B. J. Nelson, J. Puigmartí-Luis, S. Pané, *Adv. Mater.* **2019**, 1901592.
- [5] a) Y. Pan, Y. Liu, G. Zeng, L. Zhao, Z. Lai, *Chem. Commun.* **2011**, *47*, 2071; b) M. Jian, B. Liu, R. Liu, J. Qu, H. Wang, X. Zhang, *RSC Adv.* **2015**, *5*, 48433; c) C. Avci, J. Arinez-Soriano, A. Carne-Sanchez, V. Guillermin, C. Carbonell, I. Imaz, D. Maspocho, *Angew. Chem. Int. Ed.* **2015**, *54*, 14417; *Angew. Chem.* **2015**, *127*, 14625.
- [6] a) H. Kim, M. Oh, D. Kim, J. Park, J. Seong, S. K. Kwak, M. S. Lah, *Chem. Commun.* **2015**, *51*, 3678; b) X. Y. Liu, F. R. Zhang, T. W. Goh, Y. Li, Y. C. Shao, L. S. Luo, W. Y. Huang, Y. T. Long, L. Y. Chou, C. K. Tsung, *Angew. Chem. Int. Ed.* **2018**, *57*, 2110; *Angew. Chem.* **2018**, *130*, 2132.
- [7] J. Huo, L. Wang, E. Irran, H. Yu, J. Gao, D. Fan, B. Li, J. Wang, W. Ding, A. M. Amin, C. Li, L. Ma, *Angew. Chem. Int. Ed.* **2010**, *49*, 9237; *Angew. Chem.* **2010**, *122*, 9423.
- [8] W. Altermann, C. Böhmer, F. Gitter, F. Heimann, I. Heller, B. Läubli, C. Putz, *Sediment. Geol.* **2009**, *213*, 150.
- [9] a) X. Zhao, S. Liu, Z. Tang, H. Niu, Y. Cai, W. Meng, F. Wu, J. P. Giesy, *Sci. Rep.* **2015**, *5*, 11849; b) H. Li, M. M. Sadiq, K. Suzuki, P. Falcaro, A. J. Hill, M. R. Hill, *Chem. Mater.* **2017**, *29*, 6186; c) X. Zhang, Y. Liu, Y. Jiao, Q. Gao, X. Yan, Y. Yang, *J. Taiwan Inst. Chem. Eng.* **2018**, *91*, 309.
- [10] Y. Guyodo, S. K. Banerjee, R. Lee Penn, D. Burleson, T. S. Berquo, T. Seda, P. Solheid, *Phys. Earth Planet. Inter.* **2006**, *154*, 222.
- [11] a) A. P. Roberts, C. R. Pike, K. L. Verosub, *J. Geophys. Res. Solid Earth* **2000**, *105*, 28461; b) C.-I. Dobrotă, A. Stancu, *J. Appl. Phys.* **2013**, *113*, 043928.
- [12] I. Panagiotopoulos, *J. Magn. Magn. Mater.* **2011**, *323*, 2148.
- [13] a) X. Wang, M. Zhu, L. K. Koopal, W. Li, W. Xu, F. Liu, J. Zhang, Q. Liu, X. Feng, D. L. Sparks, *Environ. Sci. Nano* **2016**, *3*, 190; b) H. Tüysüz, E. L. Salabaş, C. Weidenthaler, F. Schüth, *J. Am. Chem. Soc.* **2008**, *130*, 280.
- [14] a) B. Pattengale, S. Yang, J. Ludwig, Z. Huang, X. Zhang, J. Huang, *J. Am. Chem. Soc.* **2016**, *138*, 8072; b) S. Dou, C.-L. Dong, Z. Hu, Y.-C. Huang, J.-I. Chen, L. Tao, D. Yan, D. Chen, S. Shen, S. Chou, S. Wang, *Adv. Funct. Mater.* **2017**, *27*, 1702546.
- [15] a) T. E. Westre, P. Kennepohl, J. G. DeWitt, B. Hedman, K. O. Hodgson, E. I. Solomon, *J. Am. Chem. Soc.* **1997**, *119*, 6297; b) M. Wilke, F. Farges, P.-E. Petit, G. E. Brown, F. Martin, *Am. Mineral.* **2001**, *86*, 714; c) A. J. Berry, H. S. C. O'Neill, K. D. Jayasuriya, S. J. Campbell, G. J. Foran, *Am. Mineral.* **2003**, *88*, 967; d) J. M. Zhao, F. E. Huggins, Z. Feng, G. P. Huffman, *Clay. Clay Miner.* **1994**, *42*, 737.
- [16] a) G. A. Sawatzky, F. Van Der Woude, A. H. Morrish, *J. Appl. Phys.* **1968**, *39*, 1204; b) F. M. Michel, L. Ehm, S. M. Antao, P. L. Lee, P. J. Chupas, G. Liu, D. R. Strongin, M. A. A. Schoonen, B. L. Phillips, J. B. Parise, *Science* **2007**, *316*, 1726.
- [17] T. M. de Lima Alves, B. F. Amorim, M. A. M. Torres, C. G. Bezerra, S. N. de Medeiros, P. L. Gastelois, L. E. F. Outon, W. A. D. Macedo, *RSC Adv.* **2017**, *7*, 22187.
- [18] a) H. Li, M. M. Sadiq, K. Suzuki, R. Ricco, C. Doblin, A. J. Hill, S. Lim, P. Falcaro, M. R. Hill, *Adv. Mater.* **2016**, *28*, 1839; b) M. E. Silvestre, M. Franzreb, P. G. Weidler, O. Shekhah, C. Woll, *Adv. Funct. Mater.* **2013**, *23*, 1210; c) E. Coronado, G. Minguez Espallargas, *Chem. Soc. Rev.* **2013**, *42*, 1525; d) M. Kurmoo, *Chem. Soc. Rev.* **2009**, *38*, 1353; e) G. Minguez Espallargas, E. Coronado, *Chem. Soc. Rev.* **2018**, *47*, 533; f) P. Falcaro, F. Lapierre, B. Marmiroli, M. Styles, Y. Zhu, M. Takahashi, A. J. Hill, C. M. Doherty, *J. Mater. Chem. C* **2013**, *1*, 42; g) P. Falcaro, F. Normandin, M. Takahashi, P. Scopece, H. Amenitsch, S. Costacurta, C. M. Doherty, J. S. Laird, M. D. Lay, F. Lisi, A. J. Hill, D. Buso, *Adv. Mater.* **2011**, *23*, 3901; h) R. Ricco, K. Konstas, M. J. Styles, J. J. Richardson, R. Babarao, K. Suzuki, P. Scopece, P. Falcaro, *J. Mater. Chem. A* **2015**, *3*, 19822.
- [19] a) K. Liang, R. Ricco, C. M. Doherty, M. J. Styles, S. Bell, N. Kirby, S. Mudie, D. Haylock, A. J. Hill, C. J. Doonan, P. Falcaro, *Nat. Commun.* **2015**, *6*, 7240; b) H. Wang, Y. Chen, H. Wang, X. Liu, X. Zhou, F. Wang, *Angew. Chem. Int. Ed.* **2019**, *58*, 7380; *Angew. Chem.* **2019**, *131*, 7458.
- [20] J. L. Jambor, J. E. Dutrizac, *Chem. Rev.* **1998**, *98*, 2549.
- [21] a) R. M. Cornell, *Clay. Clay Miner.* **1989**, *37*, 65; b) R. Giovanoli, R. M. Cornell, *Z. Pflanzenernähr. Bodenkd.* **1992**, *155*, 455; c) S. Ayyappan, S. Mahadevan, P. Chandramohan, M. P. Srinivasan, J. Philip, B. Raj, *J. Phys. Chem. C* **2010**, *114*, 6334.
- [22] a) C. Cannas, A. Ardu, A. Musinu, L. Suber, G. Ciasca, H. Amenitsch, G. Campi, *ACS Nano* **2015**, *9*, 7277; b) T. Sugimoto, E. Matijević, *J. Colloid Interface Sci.* **1980**, *74*, 227.
- [23] R. Banerjee, A. Phan, B. Wang, C. Knobler, H. Furukawa, M. O'Keeffe, O. M. Yaghi, *Science* **2008**, *319*, 939.

Manuscript received: June 13, 2019

Accepted manuscript online: July 16, 2019

Version of record online: August 7, 2019